Journal of Al-Azhar University Engineering Sector

Vol.18, No. 69, October 2023, 951 - 972

Thermo-hydraulic Characteristics Study of The Flat Plat-Finned Heat Sink

Mohammed A. Al-Rahman[1]*, Saeed A.A. Ibrahim[2], Sayed Ahmed[2], M. Elfaisal Elrefaie1[1]

[1] Mechanical Engineering Department, Faculty of Engineering, Al-Azhar Unversity, Cairo, Egypt.

[2] Mechanical Engineering Department, Faculty of Engineering, Zagazig Unversity, Zagazig, Egypt.

*Correspondence: mohammadabdoel-rahman.18@azhar.edu.eg

Citation:

M. A. Al-Rahman, S. A. A. Ibrahim, Sayed Ahmed, M. Elfaisal Elrefaie "Thermo-hydraulic Characteristics Study of The Flat Plat-Finned Heat Sink ", Journal of Al-Azhar University Engineering Sector, vol. 18, pp. 951-972, 2023.

Received: 06 Jun 2023

Accepted: 29 August 2023

DoI:10.21608/auej.2023.215891.1379

ABSTRACT

This research paper investigates the hydraulic and thermal characteristics of a plated-finned heat sink numerically and experimentally. Numerical simulations are conducted using Ansys Fluent software and the numerical results are compared with experimental results. This study evaluates the efficiency index of a plated-finned heat sink across a wide range of Reynolds numbers (7772- 77724) and various heat sink configurations. The obtained results showed that numerical simulations are valid with a maximum error ± 18 %. Increasing the Reynolds number and number of heat sink fins improves thermal performance while increasing the Reynolds number and number of heat sink fins decreases hydraulic performance. The results also demonstrated that the heat sink with a fin number = 8 exhibited the highest efficiency index among the configurations studied. Specifically, at a Reynolds number =7,772, the efficiency index of the heat sink with a fin number = 8 increased by 32% compared to the plate-finned heat sink with a fin number = 16. The results of the study can be used to guide the development of more efficient and cost-effective heat sinks designed for cooling electronic systems.

KEYWORDS: Plate-finned heat sink, Thermo-hydraulic performance, efficiency index, and Thermal resistance.

دراسة الخصائص الحراريه والهيدروليكية لبلوعة حرارة ذات زعانف مسطحة

محمد عبدالرحمن[1]*، سعيد عبدالله[2]، سيد أحمد[2] ، محمد الفيصل الرفاعي[1]

[1]قسم الهندسة الميكانيكية، كلية الهندسة، جامعة الأزهر، القاهرة، مصر

[2]قسم الهندسة الميكانيكية، كلية الهندسة، جامعة الزقازيق، الزقازيق، مصر

***البريد الاليكتروني للباحث الرئيسي:** mohammadabdoel-rahman.18@azhar.edu.eg

الملخص العربي: -

تبحث هذه الورقة البحثية خصـــائص الهيدروليكية والحرارية لبلوعة الحرارة ذات الزعانف المســـتوية عدديًا وتجريبيًا. تم إجراء المحاكاة العددية باستخدام برنامج Ansys Fluent وتم مقارنة النتائج العددية بالنتائج التجريبية. تقيم هذه الدراسة مؤشر كفاءة بلوعة الحرارة ذات الزعانف المستوية عبر مدى واسع من أرقام رينولدز (7772-77724) وأشكال مختلفة من بلوعات الحرارة. أظهرت النتائج التي تم الحصـول عليها أن المحاكاة العددية صـالحة بحد خطأ أقصـاه ± 18٪. تؤدي زيادة عدد زعانف بلوعة الحرارة وعدد رينولدز إلى تحســين الأداء الحراري بينما تؤدي زيادة عدد زعانف بلوعة الحرارة وعدد رينولدز إلى تقليل الأداء الهيدروليكي. أظهرت النتائج أيضًا أن بلوعة الحرارة التي لها عدد زعانف = 8 أظهر أعلى مؤشر كفاءة بين أشكال بلوعة الحرارة المدروسة. على وجه التحديد، عند رقم رينولدز = 7770، ارتفع مؤشر الكفاءة لـــبلوعة الحرارة التي لها عدد زعانف = 8 بنسبة 32٪ مقارنة ببلوعة

الحرارة التي لها عدد زعانف = 16. يمكن استخدام نتائج الدراسة لتوجيه عملية تطوير بلوعات حرارة أكثر كفاءة وفعالية من حيث التكلفة مصممة لأنظمة التبريد الإلكترونية.
الكلمات المفتاحية: بلوعة الحرارة ذات الزعانف المستوية , الأداء الهيدروليكي الحراري, مؤشر الكفاءة و المقاومة الحرارية.

1. INTRODUCTION

In recent decades, there has been a significant increase in the development of electronic components. However, there was a major problem in ensuring that their temperature remained within safe operating limits between 85 and 100 ^{o}C [1,2], where the damage rate in electronic components rises by 100% when the operating temperature increases over 120 ^{o}C [3]. Heat sinks are designed to absorb and remove heat from electronic components such as CPUs, power transistors, LEDs, and other high-power devices that generate significant amounts of heat during operation. [4-8]. In general, heat sinks are typically classified based on fins shape into two groups: plate fins and pin fins. Among these, rectangular plate-finned heat sinks (PFHS) are extensively utilized in industry to mitigate heat from diverse electronic devices, this is due to their manufacturing being simple [9]. Heat sinks are commonly manufactured using materials that have high thermal conductivity, such as aluminum or copper. The studies that enhanced and optimized PFHS performance increased with the rapid development of electronic and mechanical devices.

In a numerical investigation, the optimization of fin thickness is explored [10]. The findings indicated a 10% reduction in thermal resistance under high heat flux conditions. However, it was observed that thermal resistance increased with decreases in heat flux and fin height. The performance of horizontal FPHS equipped with dual-height fins of varying heights is analyzed [11]. The researchers discovered that utilizing a dual-height plate-fin heat sink configuration in natural convection conditions could enhance thermal performance, resulting in a decrease in thermal resistance that is proportional to the heat sink's mass. The thermal-hydraulic characteristics of perforated PFHS are investigated numerically and they found that low processor temperatures are achieved using each type of perforated [12].

In experimentally studied the thermal characteristics of a flared-fin heat sink and found that the optimal number of fins was within the range of 15-18 fins and increasing the fin length led to a decrease in thermal resistance [13]. The effect of variable height fins and fin spacing on thermal characteristics and material cost are investigated numerically [14]. They found that changing fin height had minimal effect on total thermal resistance, especially for small fin spacing values. It increased both fin spacing and height and significantly reduced material cost per unit of power.

The influence of top bypass flow on the performance of PFHS is investigated through an experimental and numerical study[15]. The researchers discovered that the average heat transfer coefficient decreased by roughly 23% as the height ratio varied from 1 to 8, indicating the substantial impact of the top bypass flow. The average heat transfer coefficient initially decreased and then reached a stable state until the height ratio reached 8. Furthermore, with an increase in the height ratio from 7 to 8, the value deviation was lower than 1%, which was consistent with the heat dissipation power-optimized state.

An experimental and numerical study to analyze the thermal characteristics of a W-type fin for the vertical heat sink, examining various parameters such as fin height, fin spacing, gap

clearance, and inclined angle [16]. The researchers concluded that the W-type finned heat sink augmented air input, resulting in reduced thermal resistance. Moreover, the thermal boundary layer was thinned, and the intersection angle between the velocity direction and temperature gradient was decreased.

A numerical investigation is carried to examine the thermal characteristics of heat sinks with ripple fins [17]. The results indicated for this case, the fins provided better enhancement of heat transfer than conventional fins. The temperature at the base of the heat sink decreased by as much as 18.35 K, and the mass-specific heat transfer coefficient increased by 101.41%. Moreover, the thermal resistance decreased by 9.81%, and a mass reduction of up to 47% was observed. A combined numerical and experimental are carried to investigate the heat transfer of PFHS with a mild fin displacement [18]. The findings revealed that the heat sink with a fin displacement achieved a 30% increase in heat transfer enhancement ratio in comparison to conventional heat sinks. Furthermore, the heat sink with a fin displacement exhibited a 27.4% decrease in surface area and a 28.7% reduction in total mass.

Bayesian optimization techniques is employed to optimize the design of a PFHS equipped with a sinusoidal wavy plate fin and crosscuts [19]. The optimization was evaluated by the comprehensive thermal performance factor (TPF), which considered both the heat transfer performance and pressure drop of the heat sink. The findings revealed that the optimized design of the PFHS with a sinusoidal wavy plate fin and crosscuts achieved a 17.6% improvement in TPF. A semi-analytical model is created to anticipate the maximum net electrical power and also to optimization of the PFHS [20]. The model predicted that heat sink designs with fin thicknesses of 0.32 and 0.44 mm and fin-to-fin distances of 1 mm would provide the most favorable outcomes. These designs were predicted to maximize the net electrical power.

Despite the researchers' valuable efforts in the field, effectively dissipating generated heat, maintaining balanced temperatures for electronic components, and reducing the size, cost, and weight of heat sinks remain significant challenges. This paper investigates experimentally and numerically, the heat transfer characteristics and hydraulic characteristics of a Plate fin heat sink across a range of Reynolds numbers (Re = 7772 – 77724) and different fin numbers. The primary objective of this paper is to evaluate the optimization of the PFHS based on both its thermal and hydraulic characteristics and estimate the efficiency index of the PFHS. The study highlights the importance of considering both thermal and hydraulic characteristics in optimizing the design of PFHS. The results of the study can be used to guide the development of more efficient and cost-effective PFHS designs for electronics cooling and energy conversion systems.

2. EXPERIMENTAL SETUP

The experimental setup and measuring tools are illustrated in Fig. 1. The setup consisted of a wind tunnel as its primary component, the wind tunnel is divided into three main parts: the bell mouth, the test section, and the centrifugal fan. The air is drawn into the wind tunnel by a centrifugal fan powered by a 1 hp electric motor. The bell mouth is used to create a uniform flow of air as it enters the wind tunnel. A thermocouple was placed at the inlet of the wind tunnel to measure the air inlet temperature.

2.1.Test Section

A test section consists of a main duct made from a 6 mm thickness Plexiglas plate and assembled tightly to prevent air leakage. The main duct has a square cross-section with 125 mm sides and a 1000 mm length. PFHS is assembled with the main duct through a hole opening at the middle of the Plexiglas duct base in dimensions (100 mm x 100 mm) as shown in Fig. 2. The PFHS was made from aluminum alloy 2017, with dimensions 100 mm*100 mm*40 mm, base thickness (t_b) = 5 mm, fins height (H) = 35 mm, fins thickness (t) = 1.5 mm, and with a different fins number (N=8, N=12, and N=16). To measure the temperature distribution of the PFHS base, five T-type thermocouples (made of copper-constantan) were placed on the PFHS base, as depicted in Fig. 3.

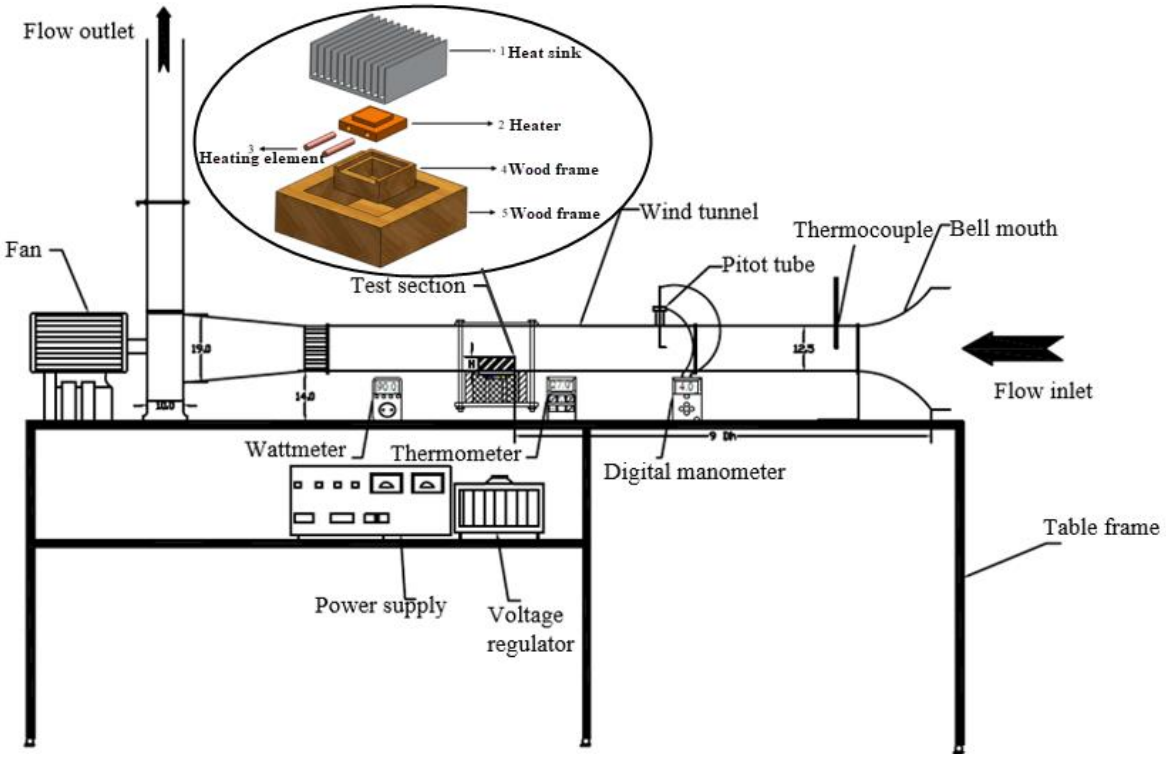

Fig. 1: Setup components and measuring tools.

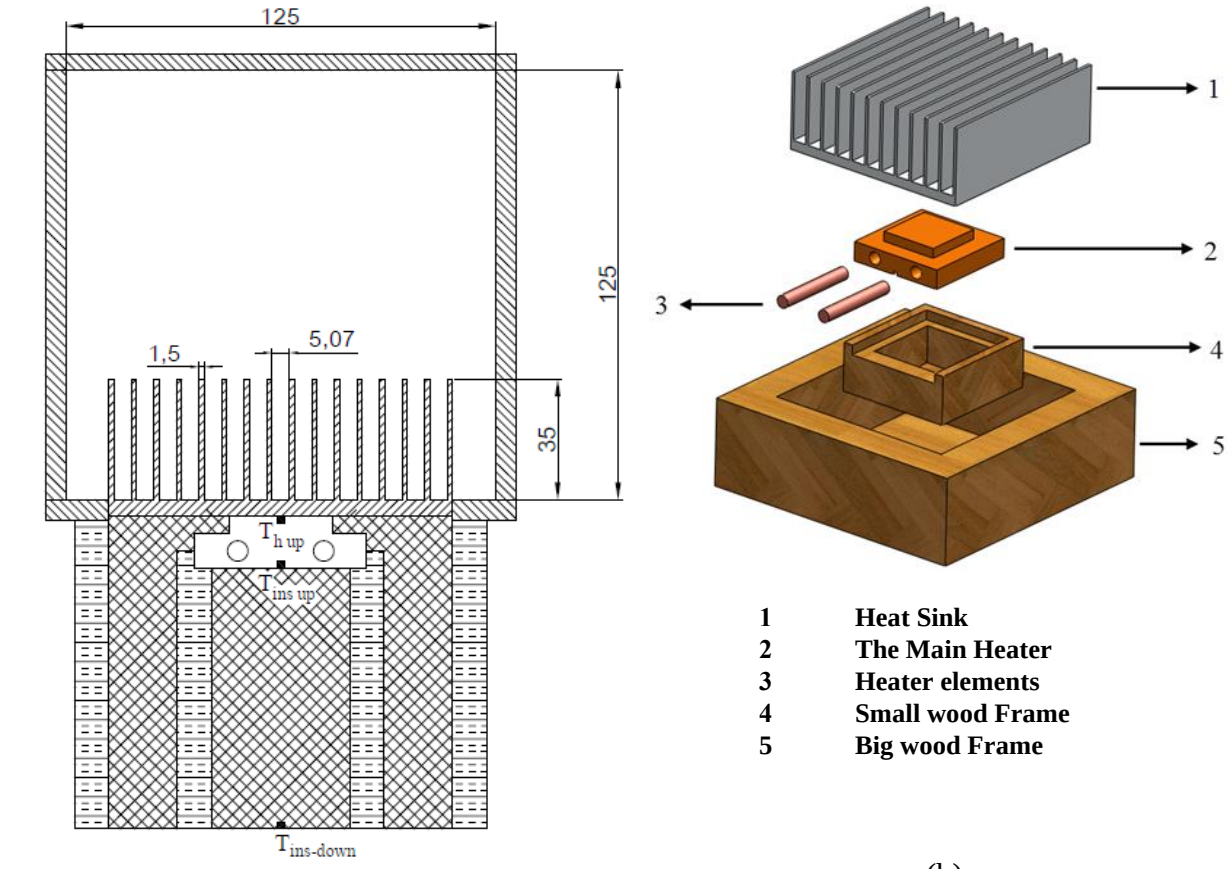

Fig. 2: Test Section Assembly, (a) Cross-section

(b) 3-D assembly.

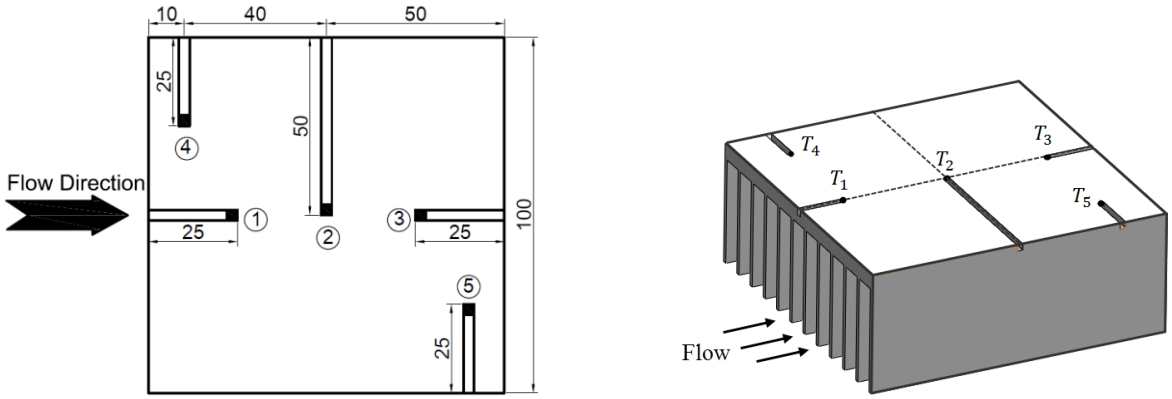

Fig. 3: PFHS configuration and thermocouples location.

(a) Plan view of PFHS. (b) 3-D of PFHS.

2.2.The Heat Source

The Heat source consists of a heater block and heater elements. The heater block is constructed from copper and has a thermal conductivity of k = 400 W/m. K. The dimensions

of the top of the heater block are 30 mm x 30 mm x 5 mm while the base dimensions are 50 mm x 50 mm x 10 mm at the base of the heater. Two electric pencil heaters, each with a power rating of 60 W, are used as the heater elements and are assembled with the heater block, as depicted in Fig. 2. To enhance the thermal coupling between the heat sink's base and the heating source, a thermal paste material with a thermal conductivity of k = 1.9 W/m. K is used. The heating source is insulated by wrapping glass wool around its sides and bottom, which has a thermal conductivity of k = 0.023 W/m. K. The heating source is then placed inside a wooden frame to minimize heat losses.

3. EXPERIMENTAL PROCEDURE

3.1.Experimental Procedure and Data Reduction.

The air velocities in the wind tunnel (U = 2, 4, 6, and 8 m/s) are determined by $U = \sqrt{\frac{2\Delta P}{\rho_a}}$ [m/s] where ΔP is pressure head [Pa], measured by a digital differential pressure manometer (Model: HD755, with range ±350 mm H_2o, and accuracy ±0.01% mm H_2o) using a pitot tube at entrance of test section and ρ_a is air density, [kg/m3]. The air velocity in the wind tunnel is controlled by a damper located at the wind tunnel outlet. The air inlet temperature ($T_a = 31 \pm 2$) is measured by using a digital thermometer (Model: OMEGA: HH21A, with range 0: 400 ℃ of type T, and accuracy ±0.1% + 0.6 ^oC) located at the wind tunnel inlet. The input electric power to the heater ($P_{input} = 30W$)is measured by a wattmeter device (Model: UT230B-EU, with range 0-3680 W, and accuracy ±1%) and adjusted via variac. The temperatures of the PFHS base (T_1, T_2, T_3, T_4, and T_5), heater temperature ($T_{h\,up}$), and insulation temperatures ($T_{ins\,up}$ and $T_{ins\,down}$) are measured at a steady state condition via a digital thermometer using thermocouples type T. The heat loss (Q_{loss}) from the heater to its surroundings via insulation may be computed using the following Equation (1):

$$Q_{loss} = K_{ins.}A\frac{T_{ins\,up} - T_{ins\,down}}{H_{ins}} \quad (1)$$

Where H_{ins} is the height of insulation = 65mm, therefore, the heating input can be obtained by Equation (2):

$$Q = P_{input} - Q_{loss} \quad (2)$$

The thermal resistance of the PFHS R_{th} can be calculated using the following Equation (3):

$$R_{th} = \frac{T_{bav} - T_a}{Q} \quad \text{where} \quad T_{bav} = \frac{\sum_{i=1}^{i=5} T_i}{5} \quad (3)$$

The overall thermal resistance $R_{th\,overall}$ can be calculated by Equation (4).

$$R_{th\,overall} = \frac{T_{h\,up} - T_a}{Q} \quad (4)$$

The Nusselt numbers Nu_{Dh} of the heat sink can be estimated by Equation (5):

$$Nu_{Dh} = \frac{h\,D_h}{K_f} \quad (5)$$

Where D_h is the hydraulic diameter of the wind tunnel estimated by $D_h = {}^{4A}/_{P}$, and h the heat transfer coefficient can be estimated by Equation (6):

$$h = \frac{Q}{A(T_{bav} - T_a)} = \frac{1}{A\,R_{th}} \quad (6)$$

K_f is the thermal conductive of the air taken at $T_{mean} = \frac{T_{bav}+T_a}{2}$

Reynolds Number (Re) calculated by Equation (7):

$$Re = \frac{U.D_h.\rho_a}{\mu_a} \quad (7)$$

and μ_a is given by Equation (8) [21]:

$$\mu_a = \mu_O \left(\frac{T_{a\,in}}{T_O}\right)^{0.7} \quad (8)$$

Stanton Number (St) is given by Equation (9):

$$St = \frac{Nu_{Dh}}{\mathrm{Re}_{Dh}.\mathrm{Pr}} \quad (9)$$

Where: Pr = Prandtl number of working fluid (air)

The efficiency index η is a parameter that relates the heat transfer and the pressure drop characteristics in heat transfer systems. Afify et al (2004) [22] proposed the following definition for the efficiency index is given by Equation (10):

$$\eta = \frac{(St\,/\,St_s)}{(\Delta P\,/\,\Delta P_s)} \quad (10)$$

Where:

$St_s = \frac{(Nu_{Dh})_s}{\mathrm{Re}_{Dh}.\mathrm{Pr}}$ Stanton number for a smooth circular tube that is equivalent to D_h ,

$(Nu_{Dh})_s = 0.023*\mathrm{Re}_{Dh}^{0.8}*\mathrm{Pr}^{0.4}$ Nusselt number for fully developed (hydro-dynamically and thermally) turbulent flow in a smooth circular tube that is equivalent to D_h [23],

$\Delta P_s = (\Delta x\,/\,D_h) f_s (0.5\rho_a U^2)$ Pressure drop [Pa] across a smooth circular tube that is equivalent to D_h ,

Δx is the distance along with ΔP_s is measured = 1 m and

$f_s = 0.316\,\mathrm{Re}_{Dh}^{-0.25}$ The friction factor for a smooth circular tube is equivalent to D_h [24].

3.2. Uncertainty Analyses.

In the current study, uncertainty analysis was performed, and the total uncertainty in derived parameter F was calculated using the following Equation (11) [25].

$$\omega_F = \sqrt{\left(\frac{\partial F}{\partial x_1}\omega_1\right)^2 + \left(\frac{\partial F}{\partial x_2}\omega_2\right)^2 + \cdots\cdots\cdots\cdots + \left(\frac{\partial F}{\partial x_n}\omega_n\right)^2} \quad (11)$$

Where ω_F is the uncertainty of the variable F, ω_1 is the uncertainty of parameter x_1, and $\frac{\partial F}{\partial x_1}$ is the partial derivative of F concerning x_1 .The measurement uncertainty and accuracy are calculated using the uncertainty of primary measurements. The convective heat transfer coefficient of a heat sink is determined by heat load and temperature measurements. The

reading uncertainty of T-type thermocouples is ±0.6°C and the wattmeter has an accuracy of ±1 %. In Equation (11), substituted in the uncertainty formula, the uncertainty of the convective heat transfer coefficient accounted for ±1.03%d. Similarly, the thermal resistance and Nusselt number accounted for ±1.03 % uncertainty in the uncertainty analysis.

4. NUMERICAL MODEL DESCRIPTION

4.1.Simulation Tools And Computational Domain

To simulate the heat transfer and airflow field for PFHS, a three-dimensional numerical investigation is carried out using the simulation software FLUENT 15.07. To simplify and hasten the computational analysis, only half of the actual test section is considered in the domain, as presented in Fig. 4. The computational domain is comprised of both fluid and solid zones. It is assumed that the flow is steady, turbulent, and incompressible. The thermo-physical characteristics of the fluid and solid materials remain constant throughout the study, as listed in Table (1). The RNG k-ε model is chosen as the turbulence model for this research due to its reliability in precisely analyzing heat transfer and flow phenomena, as demonstrated in previous studies in the same field, such as [24, 26]. Moreover, the RNG k-ε model has shown excellent agreement between experimental and numerical results. The governing equations that represent the flow field in this 3D, steady, and turbulent flow are as follows:

Continuity equation:

$$\frac{\partial}{\partial x_i}(\rho u_i) = 0 \tag{12}$$

Momentum equation:

$$\frac{\partial}{\partial x_j}\left(\rho u_i u_j\right) = -\frac{\partial P}{\partial x_i} + \frac{\partial}{\partial x_j}\left[\mu\left(\frac{\partial u_i}{\partial x_j} + \frac{\partial u_j}{\partial x_i}\right) - \frac{2}{3}\delta_{ij}\frac{\partial u_i}{\partial x_j}\right] + \frac{\partial}{\partial x_j}\left(-\rho\overline{\acute{u}_\iota \acute{u}_J}\right) \tag{13}$$

Where: $-\rho\overline{\acute{u}_\iota \acute{u}_j}$ is the Reynolds stresses defined by the Boussinesq hypothesis as Equation (14):

$$-\rho\overline{\acute{u}_\iota \acute{u}_j} = \mu_t\left(\frac{\partial u_i}{\partial x_j} + \frac{\partial u_j}{\partial x_i}\right) - \frac{2}{3}\left(\rho k + \mu_t\frac{\partial u_k}{\partial x_k}\right)\delta_{ij} \tag{14}$$

Where ρ is the density of the air, $u_i, u_j, and\ u_k$ are the mean components of velocity in three directions x, y, and z, P is the pressure, μ is the dynamic viscosity of the air, $\acute{u}$ is a fluctuating component of velocity and δ_{ij} is the Kronecker delta.

Energy Equation:

$$\frac{\partial}{\partial x_i}[\rho u_i T] = \frac{\partial}{\partial x_i}\left[(\Gamma + \Gamma_t)\frac{\partial T}{\partial x_j}\right] \tag{15}$$

Where:

Γ : is the molecular thermal diffusivity, $\Gamma = \frac{\mu}{Pr}$

Γ_t : $is\ the\ turbulent\ diffusivity, \Gamma_t = \frac{\mu_t}{Pr}$

Pr : $is\ Prandtl\ number, Pr = \frac{\mu c_p}{k}$

μ_t : is the turbulent viscosity, $\mu_t = \rho C_\mu \frac{k^2}{\varepsilon}$

i. The transport equations for k are provided by the RNG theory as Equation (16) [27,28]:

$$\frac{\partial}{\partial x_i}(\rho k u_i) = \frac{\partial}{\partial x_j}\left(\alpha_k \mu_{eff} \frac{\partial k}{\partial x_j}\right) + G_k - \rho\varepsilon \quad (16)$$

ii. The transport equations for ε are provided by the RNG theory as Equation (17) [27,28]:

$$\frac{\partial}{\partial x_i}(\rho \varepsilon u_i) = \frac{\partial}{\partial x_j}\left(\alpha_\varepsilon \mu_{eff} \frac{\partial \varepsilon}{\partial x_j}\right) + C_{1\varepsilon}\frac{\varepsilon}{k}G_k - C_{2\varepsilon}\rho\frac{\varepsilon^2}{k} - R_\varepsilon \quad (17)$$

Where**:** The turbulent kinetic energy, k is given by Equation (18):

$$k = \frac{1}{2}\left(\overline{u^2} + \overline{v^2} + \overline{w^2}\right) \quad (18)$$

The turbulence dissipation rate ε is given by Equation (19):

$$\varepsilon = \upsilon_t\left(\frac{\partial \overline{u_\iota}}{\partial x_j}\frac{\partial \overline{u_\iota}}{\partial x_j}\right) \quad (19)$$

The turbulence kinetic energy that results from the mean velocity gradients G_k is given by Equation (20):

$$G_k = -\rho\,\overline{\acute{u}_\iota \acute{u}_\jmath}\,\frac{\partial u_j}{\partial x_i} \quad (20)$$

The effective viscosity μ_{eff} is given by $\mu_{eff} = \mu + \mu_t$, the turbulent viscosity μ_t is given by: $\mu_t = \rho C_\mu \frac{k^2}{\varepsilon}$, and R_ε term in Equation (17) is given by: $R_\varepsilon = \frac{C_\mu \rho \eta^3 (1-\eta/\eta_o)}{1+\beta\eta^3}\frac{\varepsilon^2}{k}$ where $\eta_o = 4.377, \eta = \frac{k}{\varepsilon}\sqrt{2S_{ij}.S_{ij}}$ $and\ \beta = 0.012$.The constants of the transport equations of the RNG $k-\varepsilon$ model Equation (17): have the following values:

$$C_{1\varepsilon} = 1.42, C_{2\varepsilon} = 1.68, C_\mu = 0.0845, \alpha_\varepsilon = 1.393\ and\ \alpha_k = 1.393.$$

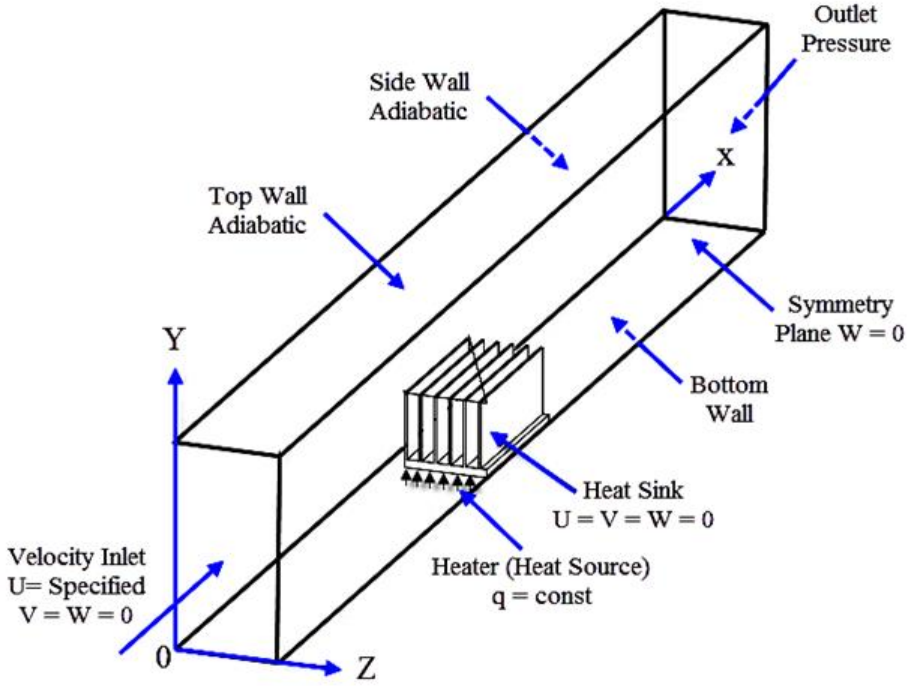

Fig. 4: The boundary conditions and computational domain for the test section.

Table (1). Materials employed in the CFD

Property	Air	Aluminum	Wood
Density, ρ (kg/m^3)	1.164	2719	720
Specific heat, C_p (J/kg.K)	1007	871	1255
Thermal conductivity, k (W/m.K)	0.02588	202.4	0.1756
Dynamic viscosity, μ (Pa.s)	1.872*10^{-5}	-	-

4.2.Boundary Conditions and Solution Settings

The inlet boundary condition for the simulation was set to a velocity-inlet, and the velocity magnitude ranged from 1 m /s to 8 m / s. The turbulence intensity was approximately 5%, and the hydraulic diameter was set at D_h= 0.125 m. The outlet boundary condition was set to a pressure-outlet boundary condition with a zero-gage pressure, and the turbulence intensity and hydraulic diameter values were assumed identical to those of the inlet boundary condition. The walls of the test section were assumed to be adiabatic, while all other walls were considered to have a no-slip condition. The working fluid used was dry air, with constant thermo-physical characteristics at 303 K. The study was carried out under steady-state conditions, and a pressure-based solver utilizing the SIMPLE scheme for pressure-velocity coupling was utilized to solve the governing equations. A second-order upwind spatial discretization was utilized for momentum, turbulent kinetic energy, and turbulent dissipation rate. To accurately monitor the solution's convergence, the residuals were set to (10^{-6}) for the energy equation and (10^{-3}) for the other equations. For this study, a constant heat flux of $(q'' = 33333.33 W/m^2)$ was applied to the heater surface, while radiation heat transfer and buoyancy/body forces were disregarded. To create a high-quality hybrid mesh, the program

GAMBIT 2.4.6 was employed, with the mesh being refined near the walls, as demonstrated in Fig. 5.

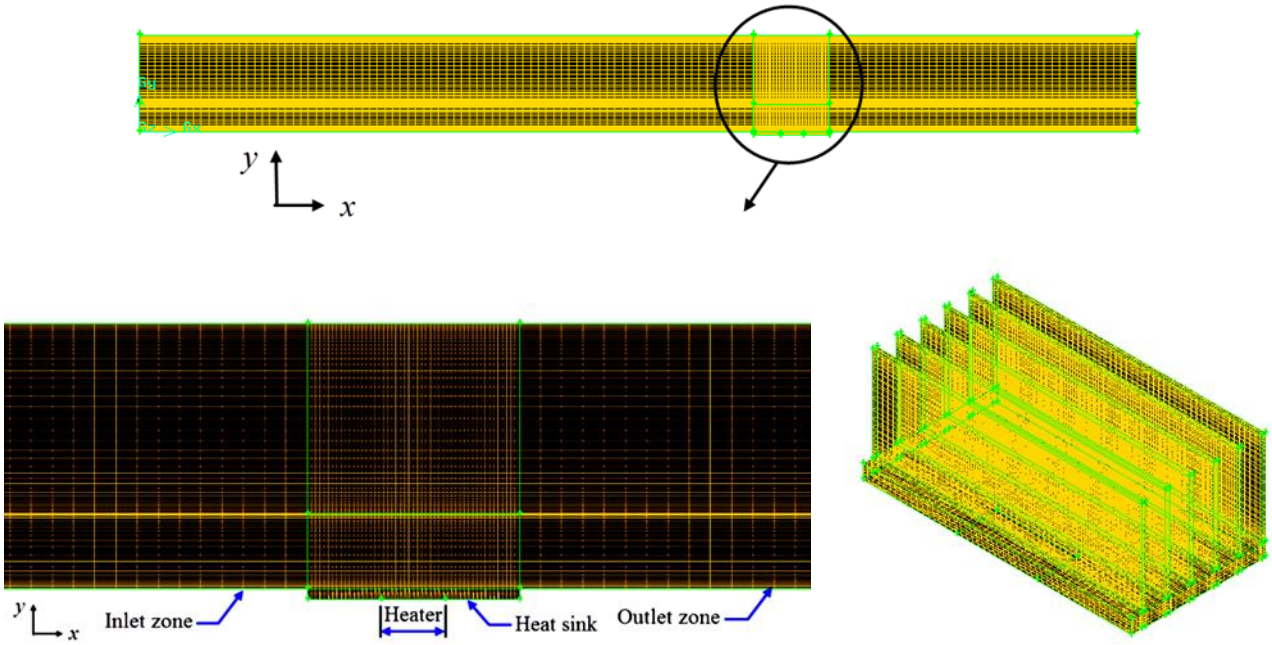

(a) **(b)**

Fig.5: Mesh configuration of the PFHS. (a) Side view of the meshed domain (b) PFHS meshing

4.3.Grid Sensitivity

In numerical analysis, grid density plays a crucial role in ensuring precise outcomes. To assess the influence of grid density on numerical results, several calculations were carried out using different mesh densities in the X, Y, and Z directions. Fig. 6. demonstrates the variations in thermal resistance with the number of grid nodes for the PFHS. The grid system used in this research was validated for PFHS with N = 16 fins and H = 35 mm at Re = 23317. As observed, the impact of grid size on computed results decreases with grids that have 311,414 nodes or more.

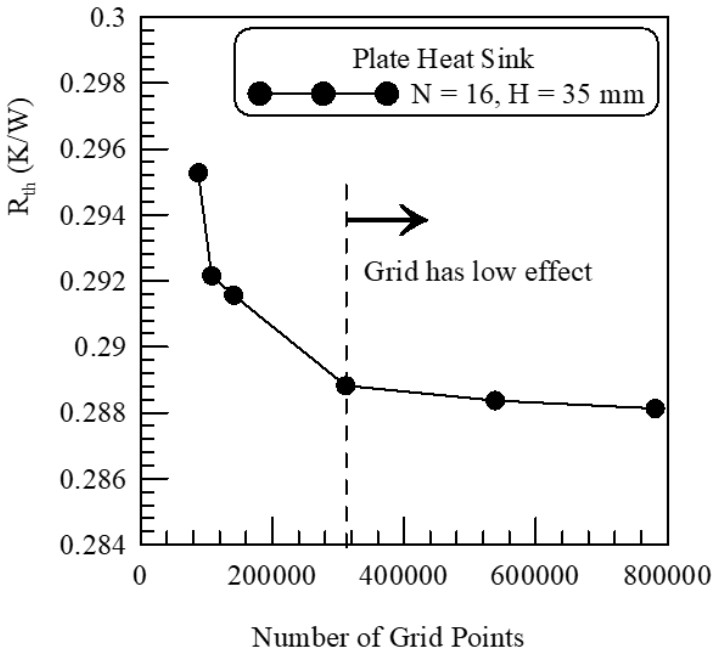

Fig. 6: Mesh independence analysis for the computational domain.

5. RESULTS AND DISCUSSION

5.1.Thermal Performance

5.1.1 Thermal Resistance of Plate-finned Heat Sink

The Re the effect on the thermal resistance of PFHS R_{th} at heat input $Q = 30W$ with different fin numbers experimentally and numerically as shown in Fig. 7. It is evident that as Re increases, the thermal resistance of the PFHS decreases because at Re increases the heat transfer coefficient by convective increase, therefore thermal resistance decreases. The slope of the curve at the low Re is higher than at the high Re, which indicates that, the effect Re decreases at the high Re. The PFHS, which has the highest fin number, provides the lowest thermal resistance because as the fin number increases the heat sink's surface area increases, therefore the thermal resistance decreases. Fig. 7 also shows the comparison between the numerical results and experimental results. From the figure, the numerical results have the same trend as the experimental results. Fig. 8 shows the validation of numerical results of thermal resistance with experimental results of thermal resistance of PFHS with N=8, 12, and 16 for several of Re. The figure shows the numerical results of the present work fitted with a maximum error of ±18% in comparison with the experimental results, this error due to loss of heat input in the experiment.

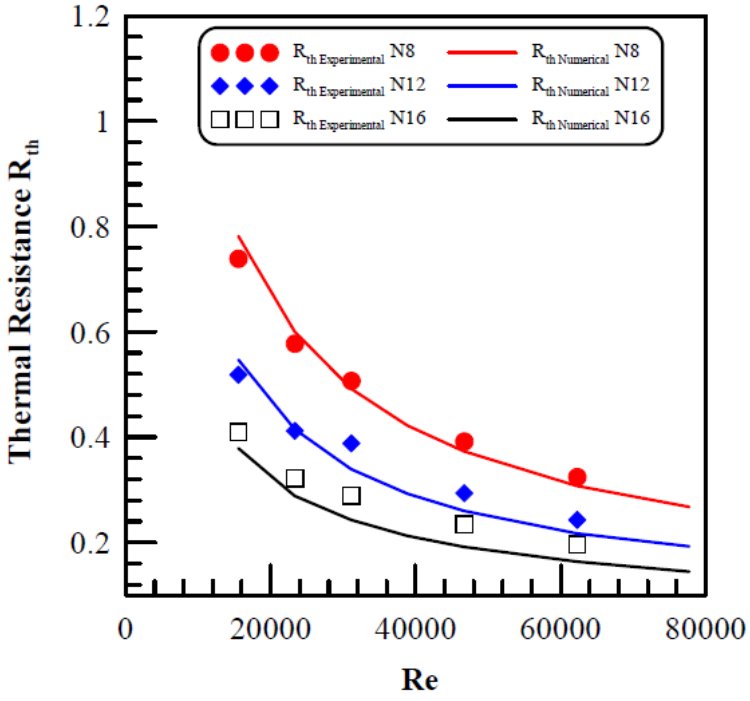

Fig. 7: Effect of Re on R_{th} of PFHS at different fins number numerical and Experimental.

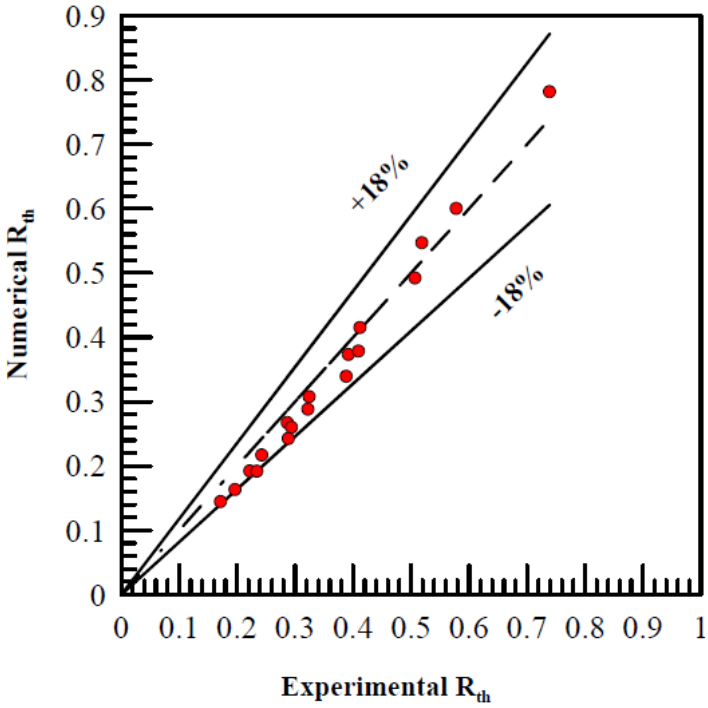

Fig. 8: Thermal resistance R_{th} from numerical and experimental for PFHS with N=8, 12, and 16 for various Re.

5.1.2 Temperature Distribution

Experimental results of temperature distribution of the PFHS base at a different number of fins, $Q = 30\ W$ and $Re = 31000$ as shown in Fig. 9, and numerically shown in Fig. (10-12). Due to the smaller area of the heater compared to the base of the heat sink, and the relatively low thermal conductivity of the heat sink, the spreading resistance of the heat sink is relatively large. This leads to the fact that the temperature distribution on the heat sink takes the shape of

a bell, where the temperature is maximum at the middle of the base and decreases towards the edges. The maximum temperature value of the heat sink base decreases as the fins number increases, where the heat sink surface area increases, and the thermal resistance reduces, therefore the rate of heat transfer is improved.

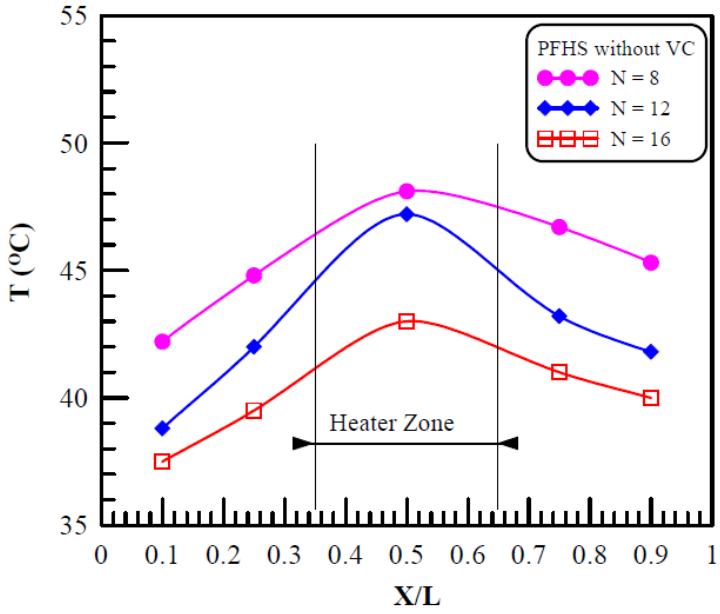

Fig.9: Experimental temperature distributions on the PFHS base.

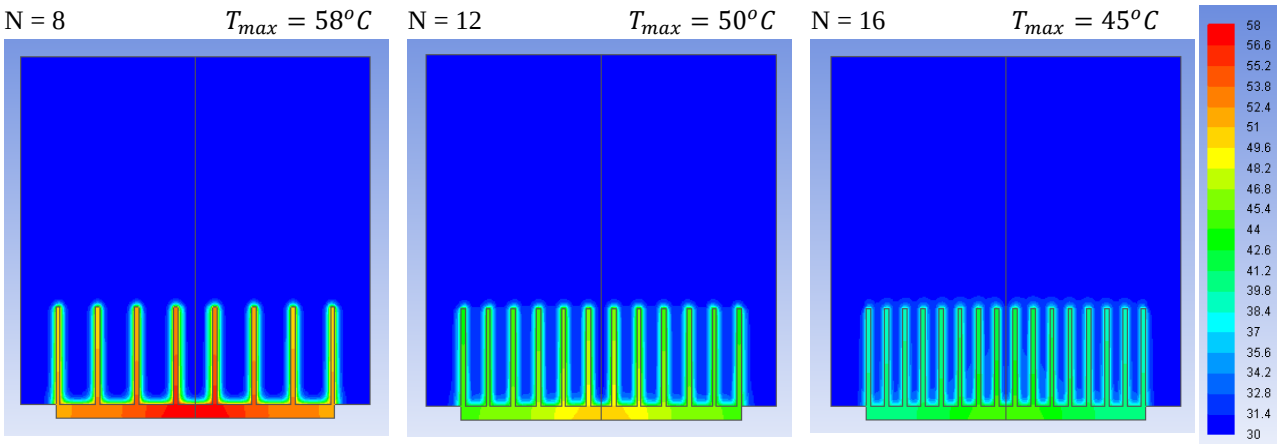

Fig. 10: Numerical temperature contours at the center of FPHS at heat input =30 and *Re* = 15545.

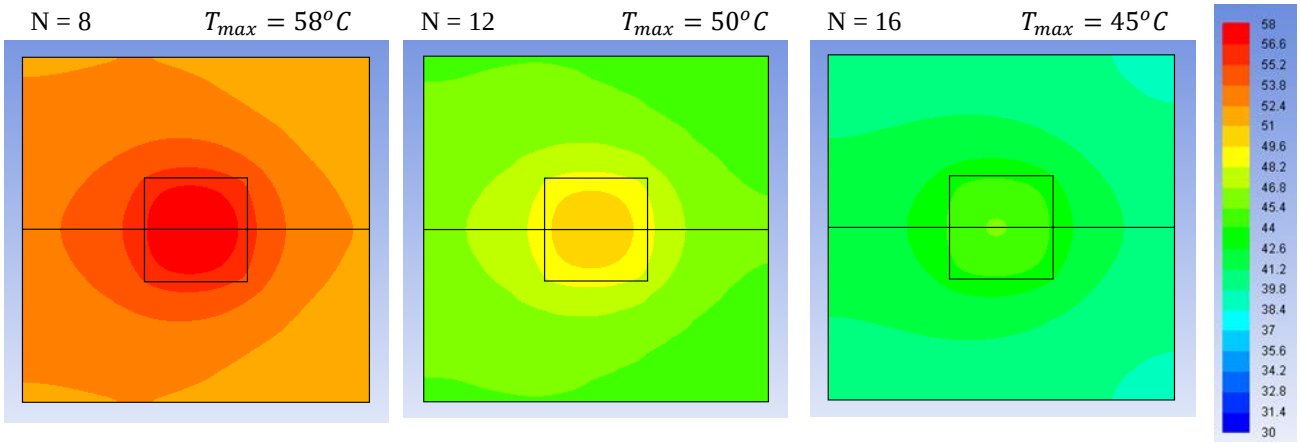

Fig.11: Numerical the temperature contours at the base of FPHS at heat input =30 W and *Re* = 15545.

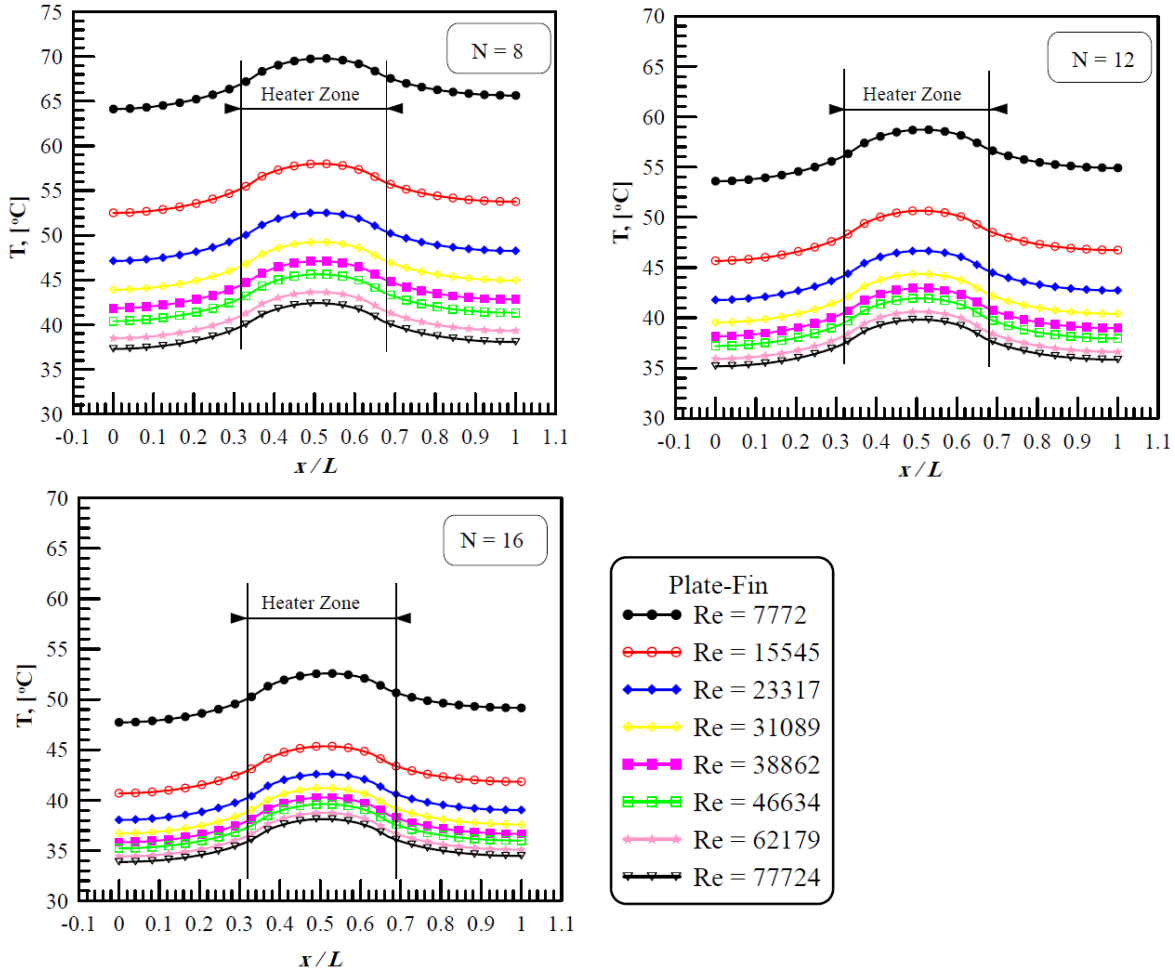

Fig.12: Numerical the temperature distributions along the centerline of PFHS base at heat input = 30W and different Re.

5.1.3 Nusselt Number

Fig. 13 illustrates the impact of fins number N on the Nusselt number Nu_{Dh} of PFHS with various Re. As shown in the figure, Nu_{Dh} was increased by increasing Re. However, Nu_{Dh} of the heat sink with $N = 16$ has a bigger value than the other heat sink, the effect of the fins number on Nu_{Dh} was very small.

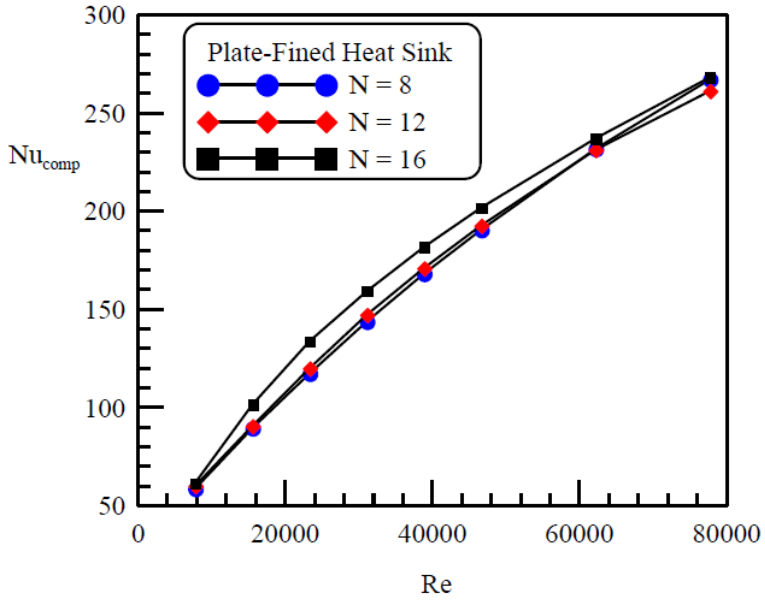

Fig. 13: The effect of fins number N on Nu_{Dh} of PFHS with various Re

5.2. Hydraulic Performance

5.2.1 Pressure Distribution

In Fig. 14, the pressure distributions along the centerline of the wind tunnel are computed numerically. When the flow passes through the PFHS, it obstructs the flow, and a vortex zone is produced behind the PFHS. The presence of a vortex zone causes a significant drop in pressure.

5.2.2 Pressure Drop

Numerically calculated pressure drops across PFHS for different Reynolds numbers and various numbers of fins are exhibited in Fig. 15. At a Reynolds number of 7,772, the pressure drops across PFHS are relatively small. However, as the Reynolds number increases, the pressure drop gradually rises because the pressure drop is proportional to the velocity's square. Furthermore, the figure indicates that the pressure drop increases as the number of fins on the PFHS increases. In contrast, the friction coefficient decreases as the Reynolds number increases because friction is inversely proportional to Reynolds, as presented in Fig. 16.

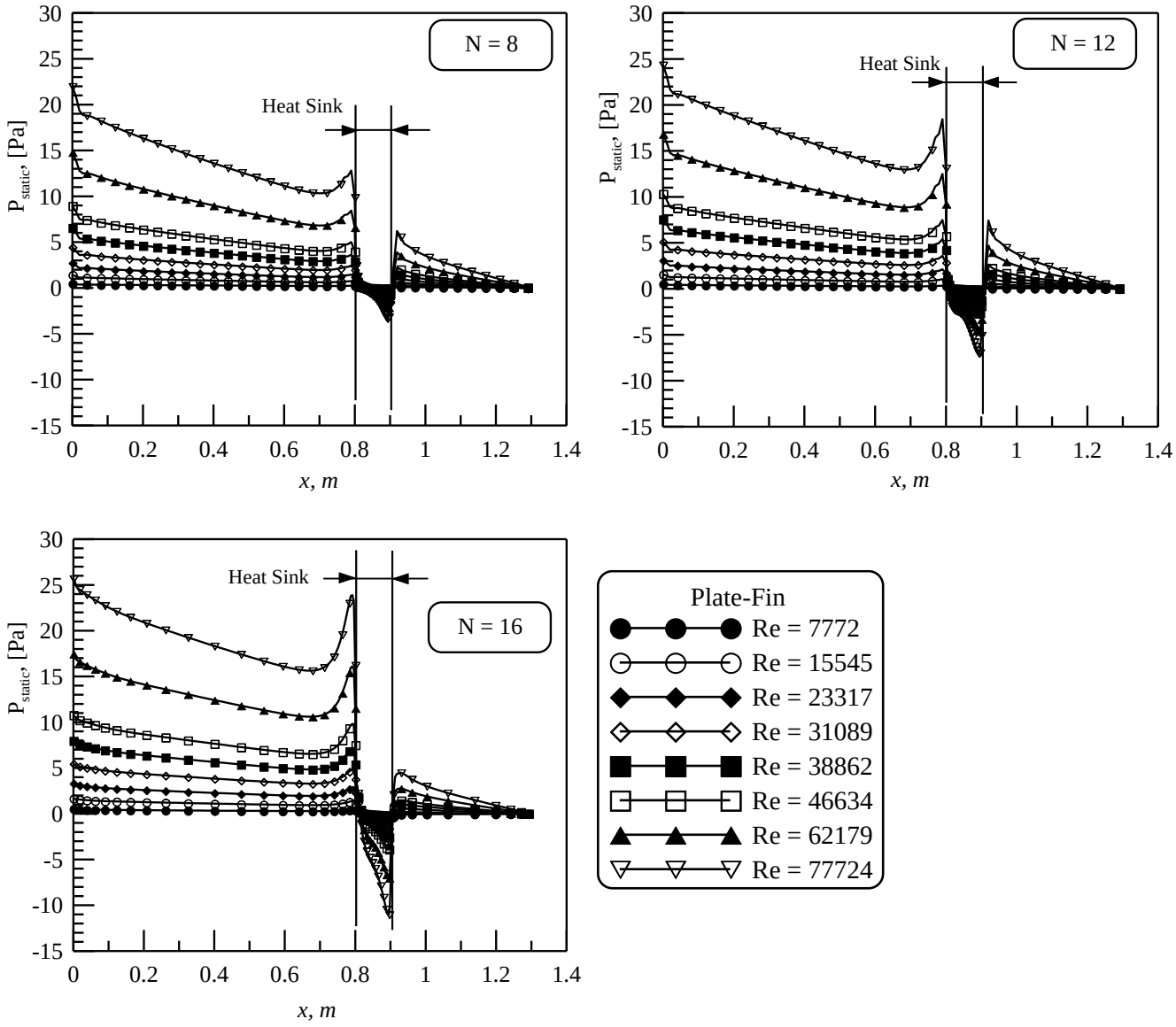

Fig. 14: Computed pressure distribution along wind tunnel centerline with using FPHS ($N = 8, 12, and\ 16$).

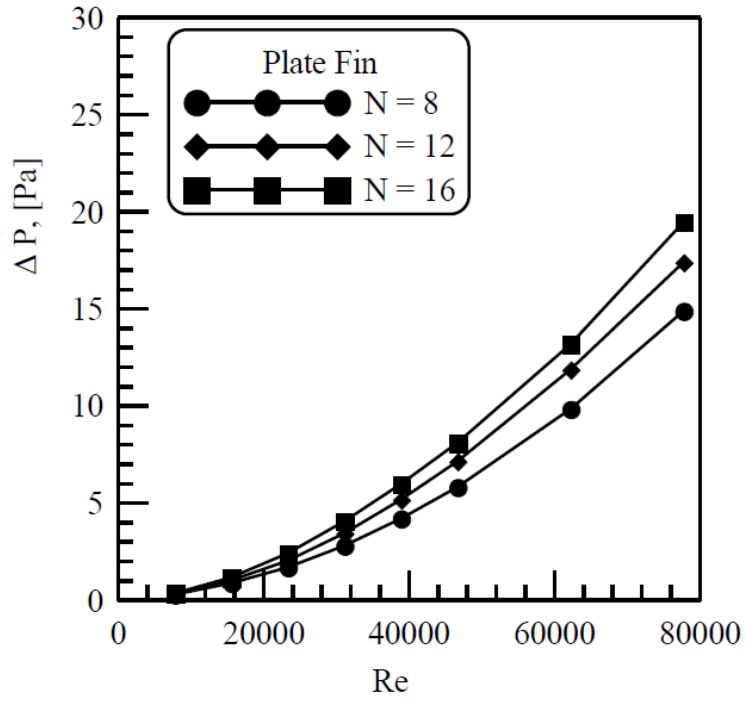

Fig. 15: Comparison of Computed Pressure Drop across PFHS with different fins number and at Various

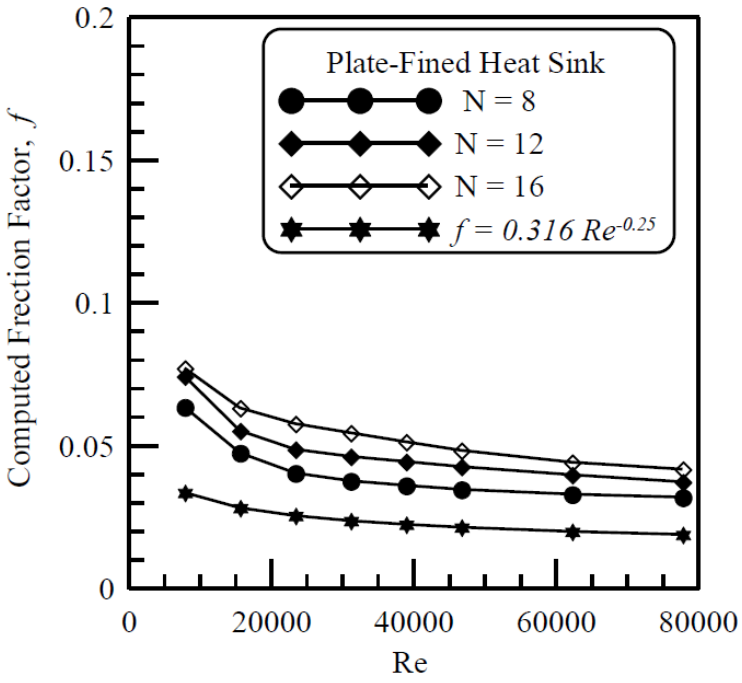

Fig. 16: Computed Friction Factor for FPHS with different fins numbers and at Various Re

6. EFFICIENCY INDEX (η)

The efficiency index η represents the correlation between the heat transfer characteristics and hydraulic characteristics for the PFHS, which is based on the relationship derived from Equation 10. Fig. 17 shows the efficiency index of PFHS at different Reynolds numbers. The efficiency index decreases as the Reynolds number increases whereas the Reynolds number increases the Stanton number decrease and the pressure drop increase this

leads to a big decrease in the efficiency index. For over the Reynolds number range, the efficiency index of the PFHS with fins number =8 has the best efficiency index. Although this PFHS has low thermal criteria but has the best hydraulic criteria.

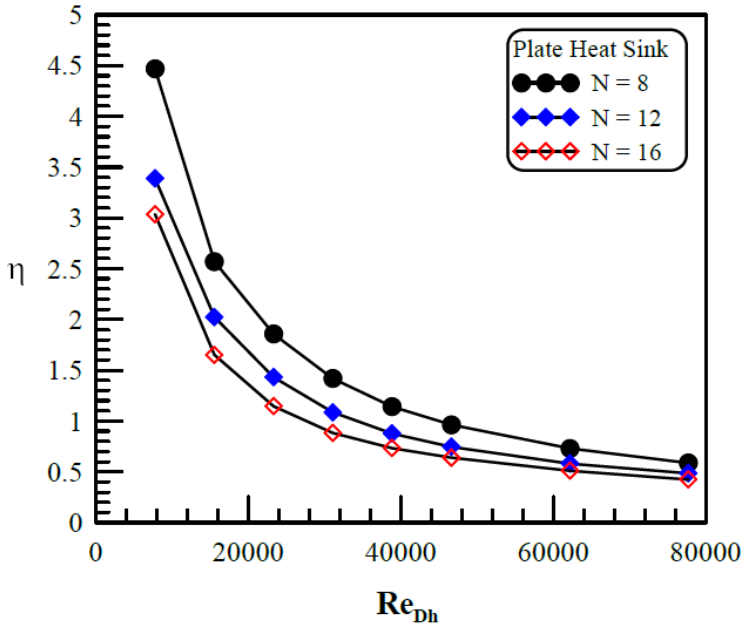

Fig. 17: Efficiency index η of PFHS with versus Re_{Dh}, and different fins number ($N = 8, 12, 16$), and heat input = 30 W.

7. CONCLUSIONS

In this study, both experimental and numerical analyses were conducted to investigate the thermal and hydraulic characteristics of a plate-finned heat sink. The research examined and presented the impact of the Reynolds number and heat sink configuration on the thermal and hydraulic performance of plate-finned heat sink. The primary findings of the study are as follows:

1. Increasing the number of fins in the plate-finned heat sink resulted in improved thermal performance. This improvement was reflected in a decrease in thermal resistance, a decrease in the temperature distribution across the base of the heat sink, and a reduction in local overheating. Additionally, the Nusselt number increased, indicating enhanced heat transfer. The thermal performance increases with an increase in the Reynolds number.
2. However, increasing the number of fins in the plate-finned heat sink led to a decrease in hydraulic performance, as evidenced by an increase in pressure drop and friction factor. Similarly, increasing Reynolds numbers resulted in a reduction in hydraulic performance.
3. The efficiency index of the plated-finned heat sink was evaluated across a wide range of Reynolds numbers (7772-77724) and various heat sink configurations. The results demonstrated that the plate-finned heat sink with a fin number of 8 exhibited the highest efficiency index among the configurations studied. Specifically, at a Reynolds number of 7,770, the efficiency index of the plated-finned heat sink with a fin number of 8 increased by 32% compared to the plate-finned heat sink with a fin number of 16.

These findings provide valuable insights into the thermal and hydraulic behavior of plate-finned heat sinks and highlight the importance of fin number and Reynolds number selection in optimizing their performance. The results can guide the development of more efficient and effective plate-finned heat sink designs for various applications requiring improved cooling and heat dissipation.

NOMENCLATURE:

A	Area (m^2)	**Greek:**	
D_h	Hydraulic diameter (m)	η	Efficiency index
f	friction	μ	Viscosity (Ns/m^2)
h	Heat transfer coefficient (W/m^2. K)	ρ	Density (kg/m^3)
H	The height (m)		
k	Thermal conductivity (W/m. K)	**Subscript:**	
Nu	Nusselt numbers	a	air
P	Perimeter (m)	avg	average
P_{input}	Electric power input (W)	b	base
Pr	Prandtl number	f	fluid
ΔP	Pressure- drop (Pa)	$T_{h\,up}$	heater upper
Q	The heat input (W)	HS	Heat sink
R	Thermal resistance (^{O}C/W)	ins	Insulation
Re	Reynolds Number	$ins\ down$	Insulation-down
T	Temperature (^{O}C)	$ins\ up$	Insulation-up

REFERENCES

[1] Hamdi E. Ahmed, B.H. Salman, M.I. Ahmed, A.Sh. Kherbeet, "Optimization of thermal design of heat sinks: a review", International Journal of Heat and Mass Transfer 118 (2018) 129–153.

[2] Ravi Kandasamy, Xiang-Qi Wang, Arun S. Mujumdar," Transient cooling of electronics using phase change material (PCM)-based heat sinks", Applied Thermal Engineering 28 (2008) 1047–1057.

[3] Esam M. Alawadhi, Cristina H. Amon, "PCM thermal control unit for portable electronic devices: experimental and numerical studies", IEEE Trans. Components Packaging Technol. 26 (2003) 116–125.

[4] Deerajkumar Parthipan, Deepakkumar Rajagopal, "Comparative analysis of cross flow and jet impingement techniques of heat sink in electronics cooling", Materials Today: Proceedings 72 (2023) 3081–3088.

[5] Mehdi Bahiraei, Saeed Heshmatian, Marjan Goodarzi, Hossein Moayedi," CFD analysis of employing a novel eco-friendly nanofluid in a miniature pin fin heat sink for cooling of electronic components: Effect of different configurations", Advanced Powder Technology 30 (2019) 2503–2516.

[6] Qie Shen, Daming Sun, Ya Xu, Tao Jin, Xu Zhao, "Orientation effects on natural convection heat dissipation of rectangular fin heat sinks mounted on LEDs", International Journal of Heat and Mass Transfer 75 (2014) 462–469.

[7] Daeseok Jang, Seung-Jae Park, Se-Jin Yook, Kwan-Soo Lee, "The orientation effect for cylindrical heat sinks with application to LED light bulbs", International Journal of Heat and

Mass Transfer 71 (2014) 496–502.
[8] Vítor A.F. Costa, António M.G. Lopes , "Improved radial heat sink for led lamp cooling", Applied Thermal Engineering. 70 (2014) 131–138.
[9] Shayan Pourhemmati, Siamak Hossainpour, "Thermal improvement of the vertical plate-fin heat sink by variable fin thickness pattern and utilizing phase change material: A numerical investigation", Journal of Energy Storage 59 (2023) 106480.
[10] Dong-Kwon Kim, "Thermal optimization of plate-fin heat sinks with fins of variable thickness under natural convection", International Journal of Heat and Mass Transfer 55 (2012) 752–761.
[11] Daechan Jeon, Chan Byon, "Thermal performance of plate fin heat sinks with dual height fins subject to natural convection", International Journal of Heat and Mass Transfer 11 (2017) 1086-1092.
[12] Waleed. Al-Sallami, Amer Al-Damook, and H.M. Thompson " A numerical investigation of the thermal-hydraulic characteristics of perforated plate-fin heat sinks," International Journal of Thermal Sciences 121 (2017) 266-277
[13] Qi Luo, Penghui Li, Lanlan Cai, Xindong Chen, Han Yan, HanXing Zhu, Pengcheng Zhai, Peng Li, Qingjie Zhang," Experimental investigation on the heat dissipation performance of flared-fin heat sinks for concentration photovoltaic modules", Applied Thermal Engineering 157 (2019) 113666
[14] Xiaoming Huang, Chunyu Shi, Junhe Zhou, Lu. Xiaojian, Xu. Guoliang, "Performance analysis and design optimization of heat pipe sink with a variable height fin array under natural convection", Appl. Therm. Eng. 159 (2019), 113939.
[15] Huikun Cai, Lijun Su, Yidai Liao, Zeju Weng, "Numerical and experimental study on the influence of top bypass flow on the performance of plate fin heat exchanger", Applied Thermal Engineering. 146 (2019) 356–363.
[16] Kai Zhang, Ming-Jia Li, Fei-Long Wang, Ya-Ling He, "Experimental and numerical investigation of natural convection heat transfer of W-type fin arrays", International Journal of Heat and Mass Transfer 152 (2020), 119315.
[17] Ihssane El Ghandouri, Anas El Maakoul, Said Saadeddine, Mohamed Meziane, "Design and Numerical Investigations of Natural Convection Heat Transfer of a New Rippling Fin Shape", Applied Thermal Engineering 178 (2020) 115670.
[18] Ali Abbas, Chi-Chuan Wang, "Augmentation of natural convection heat sink via using displacement design", International Journal of Heat and Mass Transfer 154 (2020), 119757.
[19] Yu Chen, Haoran Chen, Hao Zeng, Jianjun Zhu, Kai Chen, Zhenyu Cui, Jianli Wang, " Structural optimization design of sinusoidal wavy plate fin heat sink with crosscut by Bayesian optimization", Applied Thermal Engineering 213 (2022) 118755.
[20] Toni Pujol, Ilya T'Jollyn, Eduard Massaguer, Albert Massaguer, Ivan R. Cózar, Michel De Paepe, " Design optimization of plate-fin heat sink with forced convection for single-module thermoelectric generator", Applied Thermal Engineering 221 (2023) 119866.
[21] Reda Afify, Berbish N. S., and Abdallah Gomaa "Numerical and experimental study of turbulent flow and convective heat transfer in a circular tube with disc-baffles", Engineering Research Journal Faculty of Eng., Mattaria, Egypt, 96 (2004) M37-M61
[22] Frank M. White, "Fluid Mechanics," New York: McGraw-Hill, 2003.
[23] Frank P. Incropcra, David P. Dewitt, Theodore. L. Bergman and Adrienne S. Lavine, "Fundamentals of Heat and Mass Transfer ", 6th Edition. John Wiley & Sons 2007.
[24] Warry M. Rohsenow, and Harry Y. Choi, "Heat, Mass and Momentum Transfer", Prentice-Hall, Englewood Cliffs, New Jersey. 1969.
[25] Robert J. Moffat, "Describing the uncertainties in experimental results," Experimental Thermal and Fluid Science, 1988 3-17.

[26] Zehua Hu, and Da-Wen Sun, "Predicting local surface heat transfer coefficients by different turbulent k-T models to simulate heat and moisture transfer during air-blast chilling," International Journal of Refrigeration, 24 (7) (2000) 702-717.

[27] Victor Yakhot, Steven A. Orszag, Siva Thangam, T. B. Gatski, and Charles G. Speziale, "Development of Turbulence Models for Shear Flows by a Double Expansion Technique", Physics of Fluids, 4(7) (1992) 1510-1520.

[28] H.K. Versteeg, W. Malalasekera, "An Introduction to Computational Fluid Dynamics: the Finite Volume Method", second ed., Pearson Education Ltd, 2007.